







Multicurvature viscous streaming: Flow topology and particle manipulation

Yashraj Bhosale^{a,1} , Giridar Vishwanathan^{a,1}, Gaurav Upadhyay^a , Tejaswin Parthasarathy^a, Gabriel Juarez^{a,2} , and Mattia Gazzola^{a,b,c,2} 

Edited by Howard Stone, Princeton University, Princeton, NJ; received November 13, 2021; accepted June 29, 2022

Viscous streaming refers to the rectified, steady flows that emerge when a liquid oscillates around an immersed microfeature. Relevant to microfluidics, the resulting local, strong inertial effects allow manipulation of fluid and particles effectively, within short time scales and compact footprints. Nonetheless, practically, viscous streaming has been stymied by a narrow set of achievable flow topologies, limiting scope and application. Here, by moving away from classically employed microfeatures of uniform curvature, we experimentally show how multicurvature designs, computationally obtained, give rise, instead, to rich flow repertoires. The potential utility of these flows is then illustrated in compact, robust, and tunable devices for enhanced manipulation, filtering, and separation of both synthetic and biological particles. Overall, our mixed computational/experimental approach expands the scope of viscous streaming application, with opportunities in manufacturing, environment, health, and medicine, from particle self-assembly to microplastics removal.

viscous streaming | particle manipulation | filtration | computational inertial microfluidics

The recognition that, at the microscale, small but finite inertia can be employed to manipulate flows and suspended particles has majorly impacted microfluidics (1–4). Inertial effects have been central to the development of purely passive, hydrodynamic control strategies to align (5), separate (6), concentrate (7), and mix (8) liquids, particles, and chemicals, delivering high throughputs, operational simplicity, cost-effectiveness, precision, and delicacy (biological samples) in a robust, fault-tolerant fashion. Because of these appealing features, modern inertial microfluidics has found broad application across disciplines, from engineering (9) and biology (10) to environment (11), health, and medicine (12).

Two main flow phenomena may be leveraged to harness inertia at the microscale: inertial focusing and viscous streaming. Inertial focusing relies on cross-streamline particle migration (from the competition between wall lift and shear gradient forces) and microchannel curvature variations to focus particles of given properties at key downstream locations, from which they are collected and processed (1, 3, 13). Due to its success, particularly in clinical and point-of-care settings (1, 3), inertial focusing has perhaps come to define the field of inertial microfluidics. Nonetheless, limitations remain: Indeed, inertial focusing operates over relatively large length ($\sim\mathcal{O}(10)$ cm) and time ($\sim\mathcal{O}(1)$ s) scales (2, 3, 13); it typically requires a new microchannel design every time target particles or desired manipulation function change; and its design process is time consuming and mostly reliant on trial-and-error due to the paucity of reliable, accurate, and predictive simulations (14), thus limiting opportunities for real-time modulation, localized activations, or rapid prototyping and design.

Potential solutions may be offered by viscous streaming, a complementary and perhaps overlooked inertial flow phenomenon. Viscous streaming refers to the steady, rectified flows that emerge when a fluid oscillates around a localized microfeature, typically a solid body or a bubble (15–17). Such microfeatures have the ability to concentrate stresses (18, 19), and thus distort and remodel the surrounding flow and its topology (20–23). The result is a remarkably consistent, controllable, and convenient machinery to shape both flow and particle paths. Indeed, since the flow reorganizes over short length scales (microfeature size), a spectrum of high-velocity curvatures and gradients is produced, which, in turn, generate strong inertial forces on particles (24). This allows for precise, selective manipulation over compact footprints ($\mathcal{O}(100)$ μm) at the millisecond scale ($\mathcal{O}(10^{-3})$ s) (25, 26), making streaming an efficient way to exploit inertia at the microscale.

Despite its potential, viscous streaming has been narrowly explored, with applications (8, 16, 27) overwhelmingly employing classically understood bodies of uniform curvature (cylinders, spheres) which admit only two resulting flow topologies, known as single- and double-layer regimes (28, 29). Such a limited repertoire restricts the scope of achievable

Significance

Viscous streaming, an inertial phenomenon, refers to the steady flows that emerge when a fluid oscillates around a localized microfeature. There, stresses are concentrated, remodeling surrounding flow over short time/length scales. The result is an efficient flow machinery to mix, transport, trap, or sort at the microscale. Nonetheless, classically, viscous streaming has been investigated for uniform-curvature bodies, for which only two distinct flow topologies exist, constraining its utility and scope. We combine predictive simulations and versatile experimental techniques to demonstrate how the rational design of multicurvature bodies unlocks a novel range of flow topologies, demonstrated here in compact and tunable microparticle filtration and separation devices. Overall, our technology expands viscous streaming potential, with opportunities in micromanufacturing, environment, health, and medicine.

Author contributions: Y.B., G.V., G.U., T.P., G.J., and M.G. designed research; Y.B., G.V., and G.U. performed research; Y.B., G.V., and G.U. analyzed data; and Y.B., G.V., G.U., T.P., G.J., and M.G. wrote the paper.

The authors declare no competing interest.

This article is a PNAS Direct Submission.

Copyright © 2022 the Author(s). Published by PNAS. This article is distributed under [Creative Commons Attribution-NonCommercial-NoDerivatives License 4.0 \(CC BY-NC-ND\)](https://creativecommons.org/licenses/by-nc-nd/4.0/).

¹Y.B. and G.V. contributed equally to this work.

²To whom correspondence may be addressed. Email: gjuarez@illinois.edu or mgazzola@illinois.edu.

This article contains supporting information online at <https://www.pnas.org/lookup/suppl/doi:10.1073/pnas.2120538119/-DCSupplemental>.

Published August 29, 2022.

microfluidic applications, and sits in stark contrast to inertial focusing, where, instead, the importance of boundaries (channel walls) varying in curvature has long been recognized and leveraged to expand application range and improve performance (2, 3, 14).

Only recently, computational studies have begun to explore the nexus between body curvature manipulation and streaming flow reorganization, revealing a rich variety of flow topologies and dynamics (20–22), never experimentally reported and of potential practical use. Here, we lay out a technology based on localized microfeature design, directly driven flow oscillations, and independently controlled frequencies and amplitudes, to experimentally access such numerically predicted flows. After demonstrating their existence, we showcase their potential utility in computationally engineered filtering and separation devices. Overall, this study advances our understanding of viscous streaming and paves the way for its expansion in practical settings, while contributing to bridging the gap between experimental and computational inertial microfluidics.

Results

Multiple Discrete Curvatures—The Lattice System. Toward exploring the effects of multiple body curvatures on viscous streaming, a simplified setup referred to as the lattice system is considered (21). The lattice system consists of a two-dimensional (2D) array of circular cylinders, with exactly two distinct curvatures, κ_{max} and κ_{min} , arranged in a checkerboard pattern, and immersed in an oscillatory flow of amplitude A and angular frequency ω , as shown in Fig. 1A. The center-to-center distance between adjacent cylinders is kept constant at $6.25/\kappa_{max}$ throughout the study, without loss of generality (21). This setup allows the injection of multiple, discrete body curvatures in the flow system, whose response, at small amplitudes ($A \ll 1/\kappa_{max}$), is completely specified by only two parameters: the nondimensional Stokes layer thickness $\delta_{AC}\kappa_{max} = \kappa_{max}\sqrt{\nu/\omega}$, where ν is the

fluid kinematic viscosity, and the curvature ratio $\kappa_{max}/\kappa_{min}$. Thus, by keeping κ_{max} fixed while modifying κ_{min} and ω , the effects of curvature variations ($\kappa_{max}/\kappa_{min}$) and flow conditions ($\delta_{AC}\kappa_{max}$) on streaming topology can be studied in a controlled, systematic manner. A rich phase space composed of hitherto unseen streaming flow topologies was recently discovered numerically, and underlying bifurcation mechanisms are understood via dynamical systems theory (21). To examine the potential for microfluidic applications, a realization of the lattice system is attempted in this study.

Experimental realization. To systematically access multicurvature viscous streaming regimes, an external driver is used to generate oscillatory flows within a polydimethylsiloxane (PDMS) microfluidic channel (30), sculpted with a lattice structure at its center. Three lattice systems are fabricated, consisting of rectangular arrays of 10×8 cylinders with $r_{min} = \kappa_{min}^{-1} = 287 \mu\text{m}$ and $r_{max} = \kappa_{max}^{-1} = 287, 333, \text{ and } 571 \mu\text{m}$, resulting in the curvature ratios $\kappa_{max}/\kappa_{min} \approx 1.0, 1.2, \text{ and } 2.0$.

To generate streaming flows, a loudspeaker is directly connected to a microfluidic tubing, the other end of which is inserted into the device, as shown in Fig. 1A. The vibration of the loudspeaker diaphragm generates a time-varying pressure that produces harmonic displacement of the liquid within the device, at independently controlled frequencies and amplitudes. The investigated range of flow conditions is achieved with oscillation frequencies of 50 Hz to 600 Hz. The magnitude of the oscillation amplitude A is measured using high-speed imaging of neutrally buoyant tracer particles ($d_p = 5 \mu\text{m}$) at a sufficient distance (i.e., far-field) from the cylinders in the lattice. The particle suspension is also used for visualization of the resulting flow topologies, since they faithfully follow the flow due to their low Stokes number ($St \ll 1$). For all streaming flow visualization cases, the oscillation amplitude ($A \ll \kappa_{max}^{-1}$) is small compared to the cylinder radii.

Phase space. We start with the intuitive case of the uniform-curvature lattice ($\kappa_{max}/\kappa_{min} = 1$), illustrated in Fig. 1B and C.

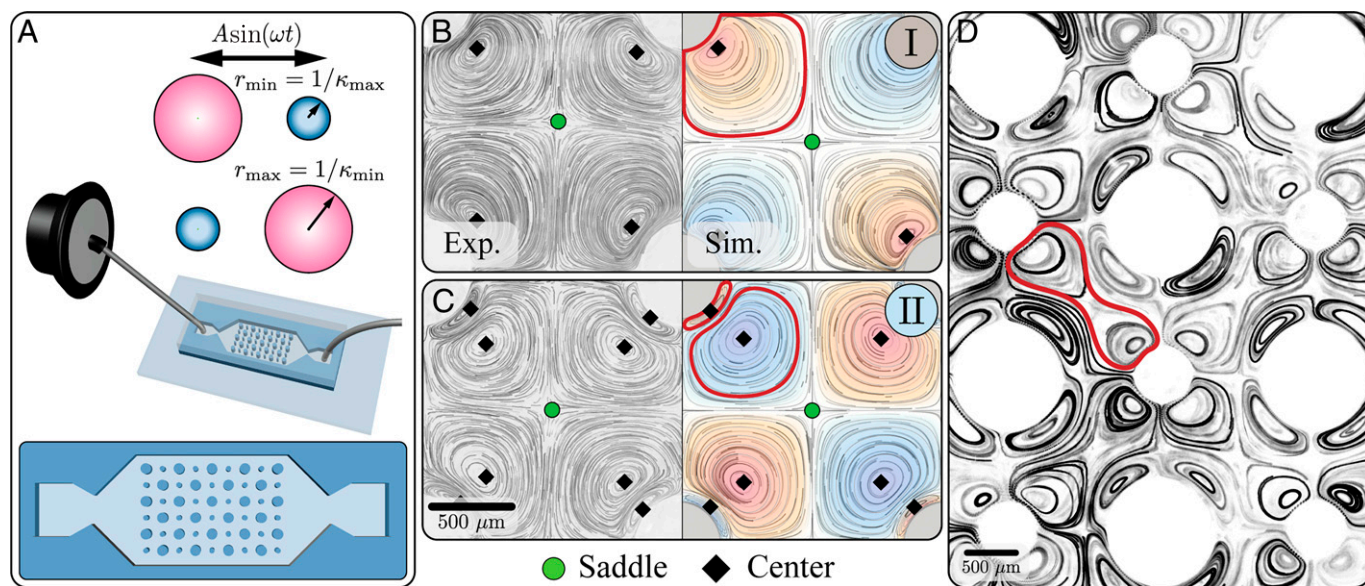


Fig. 1. Streaming flows in lattice arrays. (A) Illustration of the lattice geometry that consists of alternating cylinders. The repeating unit cell entails cylinders of two different radii, therefore curvatures κ_{max} and κ_{min} , and a fixed center-to-center spacing. The experimental setup is constituted of a glass-bonded PDMS channel connected to a loudspeaker that generates oscillatory flows along the horizontal direction. (B and C) Time-averaged particle path lines observed in experiments (Left) and simulations (Right), for a constant curvature lattice system with $\kappa_{max}/\kappa_{min} = 1$. Two distinct flow topologies, direct generalization of the well-known (B) single-layer (referred to as phase I, bordeaux outline, observed for oscillation frequency of 50 Hz, $\delta_{AC}\kappa_{max} = 0.19$) and (C) double-layer (referred to as phase II, bordeaux double outline, observed for oscillation frequency of 500 Hz, $\delta_{AC}\kappa_{max} = 0.06$) regimes are reported. The flow topologies are fourfold symmetric, and defining saddles (green circles) and centers (black diamonds) are marked. Blue represents clockwise rotation, while orange stands for counterclockwise rotation. (D) Time-averaged particle path lines observed in experiments across multiple unit cells for a lattice system with $\kappa_{max}/\kappa_{min} = 2$ and oscillation frequency of 50 Hz ($\delta_{AC}\kappa_{max} = 0.19$).

In Fig. 1 *B, Left*, observed streaming flow path lines for a unit cell are shown, while, in Fig. 1 *B, Right*, corresponding numerical streamlines are juxtaposed, with blue and orange representing clockwise and counterclockwise rotations, respectively. Of particular relevance are the flow critical points, where the velocity is zero. In 2D incompressible flows, saddles (green circles) and centers (black diamonds) conveniently offer a sparse yet complete representation of the flow field, its topology, and underlying dynamics. Further, and importantly, they are of practical use with regards to mixing, trapping, or transport. Specifically, centers are employed to attract and retain particles (31, 32), while saddles (and connecting streamlines) partition the flow, enabling particle separation (8, 25) or targeted mixing in spatially controlled chemistry (8, 27).

We first observe that the cases of Fig. 1 *B* and *C*, corresponding to $\delta_{AC}\kappa_{max} = 0.19$ and $\delta_{AC}\kappa_{max} = 0.06$, both exhibit fourfold symmetry, in line with the symmetry of the unit cell. At relatively large $\delta_{AC}\kappa_{max} > 0.1$, streaming flows result in single vortices (Fig. 1*B*, orange, outlined in bordeaux) with distinct centers, neatly separated by saddles. This topology is an expected, direct generalization of the single-layer regime for individual cylinders (28). At smaller $\delta_{AC}\kappa_{max}$, additional counterrotating outer vortices (Fig. 1*B*, blue, outlined in bordeaux) appear diagonally, squeezing the original vortices into inner bounded regions adjacent to the cylinders. This is a generalization of the double-layer regime for individual cylinders (28). As can be noticed, experiments replicate numerical solutions.

After establishing our approach in the uniform scenario, lattice systems with multiple curvatures are explored. As illustrated over six unit cells in Fig. 1*D*, a curvature ratio departure from unity ($\kappa_{max}/\kappa_{min} = 2$) breaks fourfold symmetry, leading to a twofold diagonal symmetry instead. Evidently, reduced symmetry modifies flow topology, permitting the transport of material across two of the four vortices. This is a significant breakthrough from the limitations of the uniform curvature lattice, and provides an avenue to usefully employ multiple body curvatures for sculpting, manipulating, and connecting flow regions.

Systematic variation of flow conditions ($\delta_{AC}\kappa_{max}$) and curvature ratio ($\kappa_{max}/\kappa_{min} \geq 1$) yields the computationally determined phase space of Fig. 2*A*, in which seven distinct flow topologies are identified. Here, we experimentally probe their existence (black dots), spanning curvature ratio by means of

our three lattice channels ($\kappa_{max}/\kappa_{min} = 1, 1.2$, and 2). For a given lattice, different flow topologies (phases) can be accessed by modifying $\delta_{AC}\kappa_{max}$ via the frequency ω , with low frequencies corresponding to large $\delta_{AC}\kappa_{max}$, and vice versa. The case of $\kappa_{max}/\kappa_{min} = 1$ has already been discussed, and we refer to the topologies of Fig. 1 *B* and *C* as phases I and II, respectively. Of the remaining five phases, phases III to VI are achieved with the lattice of $\kappa_{max}/\kappa_{min} = 2$, while phase VII is achieved with $\kappa_{max}/\kappa_{min} = 1.2$.

Phase III is observed for $\delta_{AC}/\kappa_{max} > 0.19$. In this phase, the inner vortices of the smaller cylinders interact with each other and form a closed connected bicentric region (marked in orange with two centers and a saddle), as shown in Fig. 2*B*. This bicentric region then separates the inner vortices (Fig. 2*B*, blue) of the larger cylinders.

Phase IV is observed when $0.1 < \delta_{AC}\kappa_{max} < 0.19$. Here, a single central vortex (orange with a center) flanked by two saddles (green) is observed, as shown in Fig. 2*C*. This central vortex then separates the inner vortices (Fig. 2*C*, blue) of the larger cylinders.

Phase V is observed when $0.07 < \delta_{AC}\kappa_{max} < 0.1$. In this case, a central vortex (orange with a center) identical to the one in phase IV is present, as shown in Fig. 2*D*. Additionally, new outer vortices (blue with centers) appear on either side of the central one, in the vicinity of the smaller cylinders.

Phase VI is seen for $\delta_{AC}\kappa_{max} < 0.07$. In this phase, a bicentric recirculation zone (orange, two centers and a saddle) is observed, as shown in Fig. 2*E*. Additionally, outer vortices (Fig. 2*E*, blue with centers) are seen on either side of this recirculation zone, around the smaller cylinders.

Phase VII is realized for $\delta_{AC}\kappa_{max} \approx 0.11$ and $\kappa_{max}/\kappa_{min} = 1.2$, and shown in Fig. 2*F*. Once again, a bicentric recirculation zone (Fig. 2*F*, orange, with two centers and a saddle) is seen, but, unlike phase VI, no outer vortices are present near the smaller cylinders.

These streaming flows are found to agree well with numerical predictions (21), thus establishing their experimental viability for potential applications. Indeed, they allow the exposure of suspended particles to a sequence of highly varied flow environments, which, in turn, can be leveraged (particularly for inertial particles, Stokes number > 0.3) to induce, hasten, or modulate cross-streamline migration for manipulation purposes. In purely oscillatory flows, and for sufficiently long time scales, all inertial

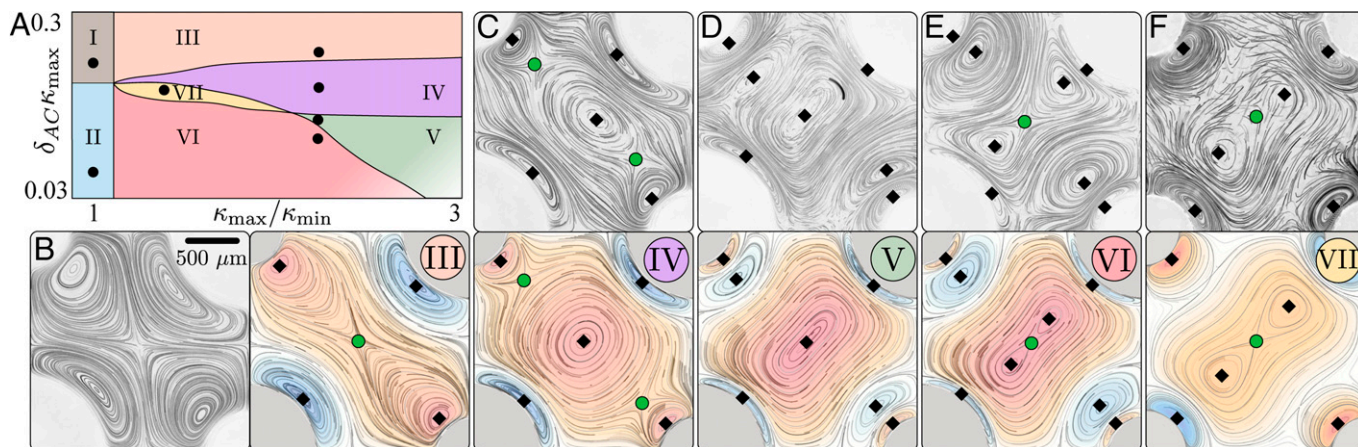


Fig. 2. Phase space of streaming flow topologies, identified through the lattice system. (A) Phase space as a function of $\delta_{AC}\kappa_{max}$ and $\kappa_{max}/\kappa_{min}$. Black lines indicate transition boundaries between phases, and black dots indicate the specific point in the phase space reported here. Streaming flows are classified into distinct phases depending on their flow topology, characterized by saddles (green circles) and centers (black diamonds). (B–F) Time-averaged particle path lines observed in experiments (*Left* in *B*, *Top* in *C–F*) and simulations (*Right* in *B*, *Bottom* in *C–F*) for distinct phases, indicated by roman numerals. Phases in *B–E* are obtained for $\kappa_{max}/\kappa_{min} = 2$, while *F* employs $\kappa_{max}/\kappa_{min} = 1.2$. Topological markers (saddles and centers) are identified and indicate good agreement between experiments and simulations.

particles are eventually trapped at vortex centers, a fact previously exploited for secure positioning (33). In the presence of commonly employed finite transport flows, however, particles' residence time in the device is limited, and trapping may or may not occur, depending on initial location, and relative strength and topology of the streaming flow. This implies that appropriate streaming patterns, perhaps enabled by our lattice system, may be better suited than others to selectively and effectively remove incoming particles from the mean flow, thus acting as contactless, compact filters, which we present next.

Particle filtration. To experimentally examine the operation of the lattice system as a filtration device, the previously described $\kappa_{max}/\kappa_{min} = 2$ lattice channel is divided into three major sections of observation, labeled as *IN*, *MID*, and *OUT* (Fig. 3A). The first zone, *IN*, refers to the inlet of the microchannel, through which a neutrally buoyant suspension of either 1) 65- μm polystyrene particles in 22% wt/wt glycerol/water solution or 2) 60- μm human buccal epithelial cells (HBECs) is injected at a volumetric flow rate of $0.1 \text{ mL} \cdot \text{min}^{-1}$. These inertial particles are tracked over a period of 50 s, and the input particle flux c_{in} across a fixed cross-section is evaluated (details in Fig. 3A legend). The second zone, *MID*, refers to the core region of the lattice system where significant trapping occurs. Finally, the third zone, *OUT*, refers to the outlet of the filter, where the output particle flux c_{out} is evaluated. Filtration efficiency is then defined as $\xi = 1 - c_{out}/c_{in}$.

Synthetic particles. Without oscillatory flow, virtually all particles pass through the lattice, and $\xi \approx 0\%$. When, instead, the filter is activated by turning the loudspeaker on, complex time-averaged flow topologies emerge from the interplay between transport flow and streaming, leading to particle retention within a few milliseconds (Fig. 3B). Indeed, as can be appreciated in Fig. 3C, inertial particles are extracted from the mean flow and captured within the streaming vortices (red arrows), a mechanism confirmed in simulations (Fig. 3D).

Filtering efficiency is then characterized via experiments and simulations as function of U_o/U_∞ , which expresses the relative strengths between streaming ($U_o = A\omega$, oscillation velocity) and transport flow (U_∞ , free-stream velocity), and $\delta_{AC}\kappa_{max}$, which determines the streaming flow topology.

Three values of $\delta_{AC}\kappa_{max}$ are chosen, corresponding to phases III, IV, and V, and, for each, U_o/U_∞ is varied from 0 to 560. Corresponding filtration efficiencies ξ are plotted in Fig. 3E, where solid circles are experimental measurements, and empty circles represent simulation results. As expected, for relatively weak streaming ($U_o/U_\infty < 100$), nearly all particles pass through the filter for any phase considered. When, instead, relative streaming strength is increased, the system response is altered. For phase III (Fig. 3E, red), filtration rate improves slowly, remaining relatively ineffective, with $\xi < 40\%$ throughout. For phases IV (Fig. 3E, purple) and V (Fig. 3E, green), instead, a sigmoid behavior is observed, whereby filtration rates improve markedly starting from $U_o/U_\infty \approx 250$ and $U_o/U_\infty \approx 100$, respectively, before (nearly) plateauing at $U_o/U_\infty \approx 560$, exhibiting average filtration efficiencies of $\xi \approx 70\%$ (phase IV), and of $\xi = 85\%$ (phase V) with peaks of $\xi = 92\%$.

When compared with simulation results (Fig. 3E, empty circles), we find that efficiency slopes are captured. We note that, for phase V, simulations predict efficiencies close to $\sim 100\%$, while experimental efficiencies are observed to saturate to an upper bound of $\xi \approx 92\%$. We attribute this mismatch to the finite size of the lattice in the channel, which departs from the periodic boundary conditions used in simulations. Streaming patterns at

the edges are therefore inevitably distorted, potentially allowing particles to leak through.

Note that a single device, upon oscillation frequency variation, generates multiple operational states, each with their own characteristic filtration performance. This variation in performance is due to the combined effect of two flow phenomena. First is the flow topology effect, where variation in frequency leads to particles experiencing varying flow velocity curvatures and accelerations. Second is the Stokes number effect, where variation in frequency leads to changes in the particle Stokes number ($St \propto \omega$). This implies a modification of the role of particle inertia, encouraging or discouraging cross-streamline migration, hence trapping. The effect of pure topology is analyzed in the next sections for the case of particle separation, whereby the use of a single streaming object allows precise assessment.

Biological particles. Post characterization of our device's performance for rigid spherical particles, we demonstrate its suitability for soft biological entities such as cells. First, we perform experiments for phase V (highest filtration efficiency) with HBECs. These cells are chosen as their size ($\sim 60 \mu\text{m}$) is comparable to the previously employed rigid particles. For HBECs, we observe $\xi \approx 82\%$, similar to that of polystyrene particles, as seen in Fig. 3E. This illustrates how, at least in the conditions tested here, particle softness or shape irregularities do not significantly impact the functioning of our streaming device.

Another critical factor, apart from filtration efficiency, is cell viability after filtration. However, HBECs directly extracted from human cheeks (cotton swabs) are already mostly dead (35), making any conclusion on viability post filtration not meaningful. Hence, to show that cells do not undergo lysis due to flow-induced shear stresses, we perform experiments using live mouse myoblasts C2C12. These cells, owing to their smaller size ($\sim 5 \mu\text{m}$ to $10 \mu\text{m}$), also experience higher shear stresses, rendering this test more demanding.

We first estimate the shear stresses experienced by synthetic/biological particles on passage through the device using order of magnitude analysis. Consider a body of length scale L immersed in an oscillatory flow (representative of our setup), with angular frequency ω , oscillation amplitude A , and dynamic viscosity μ . The shear stresses on this entity would then be of order $\mathcal{O}(\mu U_o/L)$. Substituting $U_o = A\omega$, shear stresses on the body can be estimated as $\sim \mu A\omega/L$. Upon injecting representative orders of magnitude for cell size $L \approx 10^{-5} \text{ m}$, frequency $\omega \approx 10^3 \text{ rad/s}$, viscosity $\mu \approx 10^{-3} \text{ Pa} \cdot \text{s}$, and amplitude $A \approx 10^{-4} \text{ m}$ from our setup, we obtain shear stresses on the body of $\mathcal{O}(10) \text{ Pa}$. This estimate is an order of magnitude smaller than the stresses necessary to induce cell damage (36). Hence, we conclude that the proposed device can be used with biological entities such as cells, with highly viable throughput.

To verify our analysis, we subject the C2C12 cell suspension to a flow without oscillations (positive control; Fig. 3F), and to the oscillatory flow of phase III ($\delta_{AC}\kappa_{max} = 0.2$) and phase V ($\delta_{AC}\kappa_{max} = 0.1$), for 30 min with no mean flow. A negative control was created by incubating the cells in ethanol for 10 min (Fig. 3F). It should be noted that 30 min correspond to more than 10 times the regular filtration operations. Trypan Blue (TB) exclusion test (34) performed post device operation (Fig. 3G) shows that the cells, even after experiencing streaming flows for significant amounts of time and at high frequencies (up to 400 Hz), remain highly viable ($\gtrsim 90\%$), as seen in Fig. 3H. We note that the Trypan Blue exclusion test confirms that most cells are alive after exposure to streaming, but does not rule out potential changes in cell functionality. Additional details can be found in *SI Appendix*.

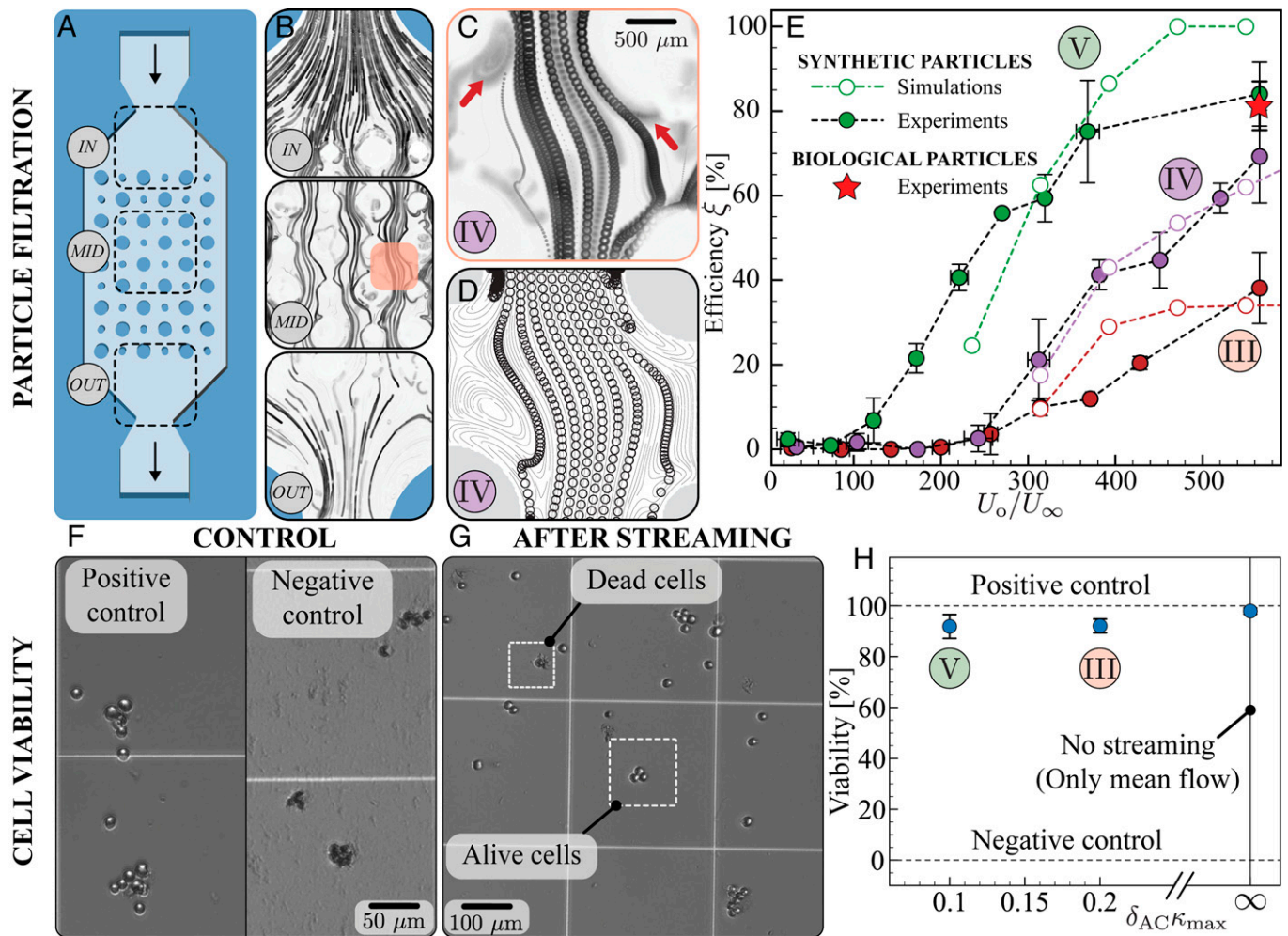


Fig. 3. Particle filtration with streaming flows in lattice arrays. (A) Illustration of the lattice array used and the locations examined for particle concentration. (B) Particle path lines observed in experiments within the device, as the particle suspension flows from inlet to outlet. The reduction in path line density, from inlet to outlet, indicates particle trapping within the device. (C and D) Example particle trajectories in (C) experiments and (D) simulations for $\kappa_{max}/\kappa_{min} = 2$, $\delta_{AC}\kappa_{max} = 0.14$ (phase IV), and $U_0/U_\infty = 310$. Particle trapping locations are indicated by red arrows. (E) Filtration efficiency $\xi = 1 - c_{out}/c_{in}$ measured experimentally (solid circles) and plotted against computational results (empty circles) for three different $\delta_{AC}\kappa_{max}$ values, corresponding to lattice phases III, IV, and V. We note that, while, in simulations, the analytical streaming condition ($A \ll \kappa_{max}^{-1}$) is always fully met, in experiments, since we fix $U_0 = A\omega$ for a particular U_0/U_∞ across phases, at low frequencies (last three points of phase III), this condition is only approximately satisfied ($A \leq \kappa_{max}^{-1}$). Nonetheless, efficiency slopes from simulations (with intercept shift along the x axis) are found to agree with experimental results. The single red star corresponds to the ξ value obtained experimentally for filtration of human cheek cells. Particle fluxes across control surfaces at the inlet (c_{in}) and outlet (c_{out}) are evaluated using standard particle tracking velocimetry. The coupled effect of flow topology (lattice phase) and particle Stokes number manifests as markedly different filtration behaviors. (F–H) Cell viability estimation for filtration through lattice arrays. (F) Control: Representative visualization of live and dead C2C12 cells on hemocytometer after Trypan Blue exclusion test (34). The cells were collected from positive control (phosphate buffer saline) and negative control (ethanol), without streaming. Cells with a bright center are alive, and are dead otherwise. (G) After streaming: Representative visualization of C2C12 cells on hemocytometer used for viability estimation using Trypan Blue exclusion test. Samples were collected from the device's outlet, after 30 mins of operation, across the frequency range 100 Hz to 400 Hz. (H) Measured viability of C2C12 cells collected from device post operation for phases III ($\delta_{AC}\kappa_{max} = 0.2$) and V ($\delta_{AC}\kappa_{max} = 0.1$). Dashed lines represent cell viability for control cases.

Overall, the proposed filtration example illustrates how the sensitivity afforded by transitioning across streaming regimes, combined with almost instantaneous (<10 ms) flow reconfiguration upon frequency ω variations, may be harnessed to dynamically control particle distributions in time and space, in a purely hydrodynamic fashion. This makes streaming a versatile and flexible mechanism, complementary to current inertial microfluidic techniques.

Having established the potential utility of multicurvature streaming via the case of discrete curvature configurations, we proceed to demonstrate a distinct microfluidic application, based on a continuous spectrum of curvatures, at the single-object level.

Continuous Curvature Variation—The Bullet System. The bullet refers to the object formed by the extrusion of a single convex

shape created by joining a semicircle of diameter $2/\kappa_{max}$ to a rounded semisquare of the same side length, as illustrated in Fig. 4A. This particular geometry was computationally designed to generate streaming features conducive to enhanced particle transport (20, 21). Here the bullet system is experimentally realized and subsequently employed for continuous particle separation.

Experimental realization. We employ the same oscillatory flow generation and channel microfabrication techniques as the lattice. The bullet is characterized by a major radius of $1/\kappa_{max} = 0.5$ mm, smoothing radius at the corners of 0.1 mm, and extrusion height of 2.5 mm. For flow streamlines visualization, a neutrally buoyant suspension of tracer particles with a diameter of 5 μ m in deionized water was used.

Phase space. Analogous to the lattice system, as $\delta_{AC}\kappa_{max}$ is decreased, distinct flow topologies emerge. We refer to them as phases 1, 2, and 3, as illustrated in Fig. 4 A–C. We emphasize

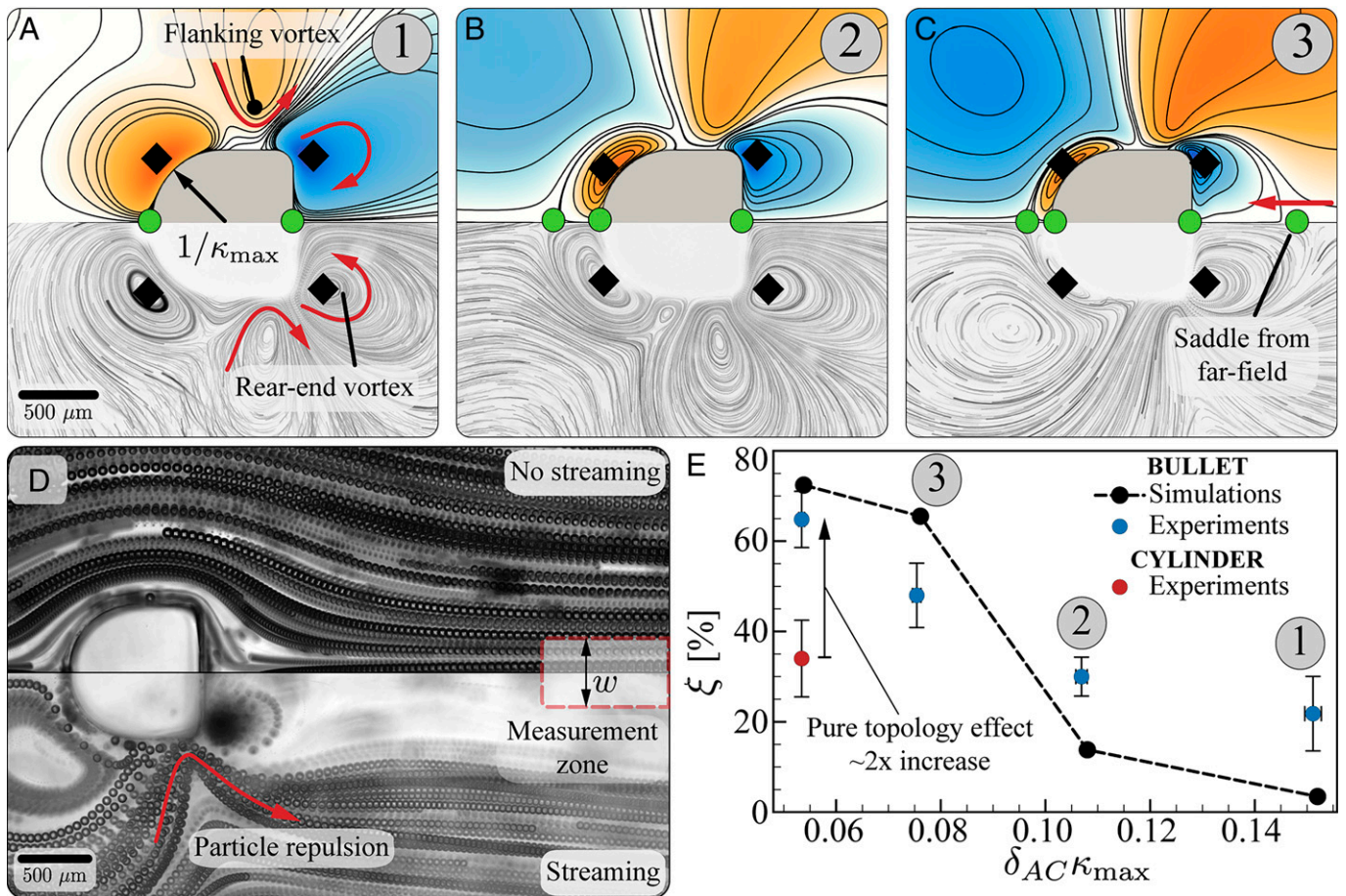


Fig. 4. Particle separation using the bullet system. (A–C) Comparison of simulated (unbounded flow domain) and experimental streaming path lines around a bullet-shaped cylinder, for phases (A) **1**, (B) **2**, and (C) **3**. (D) Demonstration of inertial separation of particles from the wake region at $\delta_{AC} \kappa_{max} = 0.05$. The width w of the measurement zone used throughout this demonstration is set to match the characteristic system's length of $500 \mu\text{m}$, corresponding to the major radius of the bullet. (E) Efficiency of particle separation $\xi = 1 - c_{out}/c_{in}$, measured experimentally (blue circles) plotted against computational results (black circles), for varying $\delta_{AC} \kappa_{max}$ and $U_o/U_\infty = 160$. The single red circle corresponds to data points obtained from particle separation experiments for a circular cylinder.

the agreement between computationally designed (top half) and experimentally realized (bottom half) flow fields.

At higher values of $\delta_{AC} \kappa_{max}$, phase **1** is observed. In this phase, a single set of vortices (center, black diamonds), which resemble the inner vortices observed for a circular cylinder, are seen on the circular front end, as shown in Fig. 4A. On the square rear end, due to the large curvature mismatch at the corners, a set of vortices of large size and flow strength is obtained. In addition to these rear-end vortices, a new set of outer vortices flank the bullet sides. Decreasing $\delta_{AC} \kappa_{max}$ results in phase **2**. In this phase (Fig. 4B), the original set of vortices at the circular front end reconfigures as inner bounded vortices (thickness defined by green saddles), surrounded by outer counterrotating vortices, similar to the double-layer regime of a circular cylinder. Additionally, a well-defined boundary appears between inner vortices on the circular front end and flanking vortices. By further decreasing $\delta_{AC} \kappa_{max}$, the system transitions to phase **3** (Fig. 4C), where the square-end vortices become bounded by the saddle approaching from the far field. Consequently, flanking vortices increase in strength and curvature near the rear end.

The bullet illustrates how computational prototyping enables new and specialized sets of flow topologies, via microfeature design. We anticipate that, upon application of a left-to-right transport flow, the flanking vortices will be effective in laterally deflecting incoming particles. Additionally, the rear vortices are expected to trap remaining undeflected particles, rendering the

bullet well suited for continuous separation, which we present next.

Particle separation. To experimentally demonstrate particle separation, a steady transport flow laden with $65\text{-}\mu\text{m}$ neutrally buoyant, inertial particles is generated past the bullet, such that the direction of flow is from the circular end toward the square end. Particle separation is then activated by superimposing streaming onto a mean transport flow of $0.2 \text{ mL} \cdot \text{min}^{-1}$. This results in the example flow topology of Fig. 4D. As particles are convected around the bullet, they encounter the flanking vortices, which, as predicted, are observed to deflect particles aside. Any remaining particle that makes it to the square end of the bullet is then readily trapped by the rear vortices. This creates a downstream region mostly free from particles, referred to as the separation zone. We emphasize the contrast between streaming application and lack thereof, illustrated in Fig. 4D.

Quantification of particle separation is performed similarly to the lattice system, where particles are now tracked in a measurement zone (marked to scale in Fig. 4D) before and after streaming is applied. Here, separation efficiency $\xi = 1 - c_{out}/c_{in}$ refers to the number of particles that flow in the measurement zone (c_{out}) relative to the unperturbed (i.e., no streaming) reference particle content (c_{in}), and depends once again on U_o/U_∞ and $\delta_{AC} \kappa_{max}$. For the fixed value $U_o/U_\infty = 160$, the efficiency ξ is plotted as a function of $\delta_{AC} \kappa_{max}$ in Fig. 4E. As can be seen, different behaviors emerge across phases, with phase **3** being

evidently superior ($\xi > 70\%$), relative to the modest performance of phase 1 ($\xi \approx 20\%$).

We attribute this difference to the bounded and stronger rear-end vortices of phase 3, accompanied by stronger flanking vortices. On the other hand, because oscillation frequencies increase from phase 1 to phase 3, the Stokes number accordingly increases from $St = 0.043$ to $St = 0.351$. This implies a higher propensity of particles in phase 3 to cross streamlines, potentially favoring trapping and aiding separation. To isolate the effect of flow topology, we consider additional experiments involving streaming circular cylinders. This allows us to match phase 3 frequency and Stokes number, while attaining an entirely different flow topology, the well-known double-layer structure of Fig. 1C. As can be seen in Fig. 4E, the bullet outperforms the circular cylinder by a factor of 2, confirming the role of flow topology and the utility of our multicurvature design approach. Additional details can be found in *SI Appendix*. Finally, we note the qualitative agreement with simulations, whereby efficiency trends are captured.

Conclusion. This study revisits viscous streaming from a fundamental fluid mechanics perspective, asking whether classical streaming flow topologies may be remodeled and expanded into a richer and useful repertoire. By combining simulations and experiments, we show that immersed microfeature design involving multiple curvatures is effective in dictating a variety of complex flows. This multicurvature approach is illustrated both in a discrete sense, for collections of objects (lattice), and in a continuous sense, at the single-object level (bullet). Potential for practical application is explored in particle filtration and separation devices. In both cases, a single design generates, upon oscillation frequency variation, a range of distinct flow topologies, each characterized by different manipulation properties and accessible within milliseconds (< 10 ms). This renders the systems versatile and primed for real-time control and operation. Additionally, our prototypes are shown to be effective at filtration (up to 92%) and clearing (up to 75%), despite the absence of an explicit engineering optimization effort. Importantly, these systems are capable of handling both synthetic and biological particles, the latter maintaining high viability rates. All in all, this study provides the computational and technological tools, as well as understanding, to expand the use of viscous streaming beyond its current niche set of applications, thus taking full advantage of associated vigorous inertial effects, rapid activation, spatial and temporal control, and modularity, synergistically with mainstream inertial microfluidics.

Materials and Methods

Simulation Method and Numerical Implementation. We briefly recap the governing equations and the numerical solution technique. We consider incompressible viscous flows in a periodic (lattice) or unbounded (bullet) domain Σ . In this fluid domain, immersed solid bodies perform simple harmonic oscillations. The bodies are density matched and have support Ω and boundary $\partial\Omega$. The flow can then be described using the incompressible Navier-Stokes equations Eq. 1,

$$\nabla \cdot \mathbf{u} = 0; \quad \frac{\partial \mathbf{u}}{\partial t} + (\mathbf{u} \cdot \nabla) \mathbf{u} = -\frac{\nabla P}{\rho} + \nu \nabla^2 \mathbf{u}, \quad \mathbf{x} \in \Sigma \setminus \Omega, \quad [1]$$

1. D. Di Carlo, D. Irimia, R. G. Tompkins, M. Toner, Continuous inertial focusing, ordering, and separation of particles in microchannels. *Proc. Natl. Acad. Sci. U.S.A.* **104**, 18892–18897 (2007).
2. D. Di Carlo, Inertial microfluidics. *Lab Chip* **9**, 3038–3046 (2009).
3. J. M. Martel, M. Toner, Inertial focusing in microfluidics. *Annu. Rev. Biomed. Eng.* **16**, 371–396 (2014).
4. J. Zhang *et al.*, Fundamentals and applications of inertial microfluidics: A review. *Lab Chip* **16**, 10–34 (2016).
5. E. Ozkumur *et al.*, Inertial focusing for tumor antigen-dependent and -independent sorting of rare circulating tumor cells. *Sci. Transl. Med.* **5**, 179ra47 (2013).
6. C. Wang, S. V. Jalikop, S. Hilgenfeldt, Size-sensitive sorting of microparticles through control of flow geometry. *Appl. Phys. Lett.* **99**, 034101 (2011).

where ρ , P , \mathbf{u} , and ν are the fluid density, pressure, velocity, and kinematic viscosity, respectively. The dynamics of the fluid-solid system is coupled via the no-slip boundary condition $\mathbf{u} = \mathbf{u}_s$, where \mathbf{u}_s is the solid body velocity. The system of equations is then solved using a velocity-vorticity formulation with a combination of remeshed vortex methods and Brinkmann penalization (37). This method has been validated across a range of flow-structure interaction problems, from flow past bluff bodies to biological swimming (37–42). Recently, the accuracy of this method has been demonstrated in rectified flow contexts as well, capturing steady streaming responses from arbitrary rigid shapes in 2D and 3D (20–22). Lastly, the motion of inertial particles demonstrated in the lattice trapping and bullet separation sections is captured using the Maxey-Riley equations (43).

Experimental Methods. The channels were fabricated using PDMS (Sylgard 184, 10:1 resin:cross-linker) molded from a Computer Numerical Control micro-machined aluminum mold, pretreated with silicone mold release spray. The PDMS was cleaned with isopropanol, perforated, and then bonded to a glass slide after oxygen plasma treatment for 2 min. Polyethylene tubing (PE 200, inner diameter 1.5 mm, outer diameter 1.9 mm) was inserted at the inlet and outlet.

Sinusoidal oscillatory flow of frequencies ranging from 50 Hz to 600 Hz was produced at the outlet by an external oscillatory driver generated by a loudspeaker diaphragm. Details of the generation and fidelity of oscillatory flow are reported elsewhere (30). Bright-field microscopy with $2\times$ and $4\times$ objective lenses (depth of field 125 μm) was used to image tracer particles at the channel midplane. Frame rates between 1 fps and 20 fps were used with an exposure time of 100 μs to minimize streaking.

For flow visualization experiments, polystyrene particles with a diameter of 5 μm were suspended in deionized water. For particle manipulation experiments, polystyrene particles with a diameter of 65 μm were suspended in a solution of 22% (wt/wt) glycerol and deionized water with a density and kinematic viscosity of $\rho = 1.15 \text{ kg/m}^3$ and $\nu = 1.68 \text{ mm}^2/\text{s}$, respectively, and remained neutrally buoyant. The choice of particle suspension is based on the magnitude of the particle Reynolds number and the Stokes number. The particle Reynolds number is defined as $Re_p = A\omega\kappa_{max}d_p^2/4\nu$, and the Stokes number is defined as $St = \rho_p\omega d_p^2/18\mu$. Here, A and ω are the oscillation amplitude and angular frequency, κ_{max} is the maximum curvature of the immersed microfeature, d_p is the particle diameter, ρ_p is the density of the particle, and μ and ν are the fluid's dynamic and kinematic viscosity, respectively. For the frequency range used in our experiments, and for 5- μm particles, we have $Re_p \ll 0.1$ and $St \ll 0.1$, while, for 65- μm particles, values are larger but still less than unity ($Re_p < 1$ and $St < 1$). See *SI Appendix* for tabulated values of Re_p and St .

Data, Materials, and Software Availability. All study data are included in the article and/or supporting information. This work used the Extreme Science and Engineering Discovery Environment (XSEDE) Stampede2 (44).

ACKNOWLEDGMENTS. We thank S. Hilgenfeldt for helpful discussions over the course of this work. We thank Taher Saif for the generous gift of the C2C12 cell line used in particle filtration. We acknowledge support by the NSF under NSF CAREER Award #CBET-1846752 (M.G.) and the NSF Expedition Award "Mind in Vitro" #CISE-2123781 (M.G.). This work used XSEDE Stampede2, supported by NSF Grant ACI-1548562, at the Texas Advanced Computing Center through Allocation TG-MCB190004.

Author affiliations: ^aMechanical Science and Engineering, University of Illinois at Urbana-Champaign, Urbana, IL 61801; ^bNational Center for Supercomputing Applications, University of Illinois at Urbana-Champaign, Urbana, IL 61801; and ^cCarl R. Woese Institute for Genomic Biology, University of Illinois at Urbana-Champaign, Urbana, IL 61801

7. S. Ookawara, N. Oozeki, K. Ogawa, P. Löb, V. Hessel, Process intensification of particle separation by lift force in arc microchannel with bifurcation. *Chem. Eng. Process.* **49**, 697–703 (2010).
8. B. R. Lutz, J. Chen, D. T. Schwartz, Microfluidics without microfabrication. *Proc. Natl. Acad. Sci. U.S.A.* **100**, 4395–4398 (2003).
9. J. Seo, M. H. Lean, A. Kole, Membrane-free microfiltration by asymmetric inertial migration. *Appl. Phys. Lett.* **91**, 033901 (2007).
10. M. Masaali *et al.*, Continuous inertial focusing and separation of particles by shape. *Phys. Rev. X* **2**, 031017 (2012).
11. A. Schaap, T. Rohrlack, Y. Bellouard, Lab on a chip technologies for algae detection: A review. *J. Biophotonics* **5**, 661–672 (2012).

12. A. J. Mach, D. Di Carlo, Continuous scalable blood filtration device using inertial microfluidics. *Biotechnol. Bioeng.* **107**, 302–311 (2010).
13. B. Miller, M. Jimenez, H. Bridle, Cascading and parallelising curvilinear inertial focusing systems for high volume, wide size distribution, separation and concentration of particles. *Sci. Rep.* **6**, 36386 (2016).
14. S. Razavi Bazaz *et al.*, Computational inertial microfluidics: A review. *Lab Chip* **20**, 1023–1048 (2020).
15. M. S. Longuet-Higgins, Viscous streaming from an oscillating spherical bubble. *Proc. Royal Soc. London. Ser. A Math. Phys. Eng. Sci.* **454**, 725–742 (1998).
16. B. R. Lutz, J. Chen, D. T. Schwartz, Microscopic steady streaming eddies created around short cylinders in a channel: Flow visualization and stokes layer scaling. *Phys. Fluids* **17**, 023601 (2005).
17. C. Wang, S. V. Jalikop, S. Hilgenfeldt, Efficient manipulation of microparticles in bubble streaming flows. *Biomicrofluidics* **6**, 012801 (2012).
18. P. Marmottant, S. Hilgenfeldt, Controlled vesicle deformation and lysis by single oscillating bubbles. *Nature* **423**, 153–156 (2003).
19. P. Marmottant, S. Hilgenfeldt, A bubble-driven microfluidic transport element for bioengineering. *Proc. Natl. Acad. Sci. U.S.A.* **101**, 9523–9527 (2004).
20. T. Parthasarathy, F. K. Chan, M. Gazzola, Streaming-enhanced flow-mediated transport. *J. Fluid Mech.* **878**, 647–662 (2019).
21. Y. Bhosale, T. Parthasarathy, M. Gazzola, Shape curvature effects in viscous streaming. *J. Fluid Mech.* **898**, A13 (2020).
22. F. K. Chan, Y. Bhosale, T. Parthasarathy, M. Gazzola, Three-dimensional geometry and topology effects in viscous streaming. *J. Fluid Mech.* **933**, A53 (2022).
23. Y. Bhosale, T. Parthasarathy, M. Gazzola, Soft streaming – flow rectification via elastic boundaries. *J. Fluid Mech.* **945**, R1 (2022).
24. S. Agarwal, F. K. Chan, B. Rallabandi, M. Gazzola, S. Hilgenfeldt, An unrecognized inertial force induced by flow curvature in microfluidics. *Proc. Natl. Acad. Sci. U.S.A.* **118**, e2103822118 (2021).
25. R. Thameem, B. Rallabandi, S. Hilgenfeldt, Particle migration and sorting in microbubble streaming flows. *Biomicrofluidics* **10**, 014124 (2016).
26. R. Thameem, B. Rallabandi, S. Hilgenfeldt, Fast inertial particle manipulation in oscillating flows. *Phys. Rev. Fluids* **2**, 052001 (2017).
27. B. R. Lutz, J. Chen, D. T. Schwartz, Characterizing homogeneous chemistry using well-mixed microeddies. *Anal. Chem.* **78**, 1606–1612 (2006).
28. J. Holtmark, I. Johnsen, T. Sikkeland, S. Skavlem, Boundary layer flow near a cylindrical obstacle in an oscillating, incompressible fluid. *J. Acoust. Soc. Am.* **26**, 26–39 (1954).
29. C. Lane, Acoustical streaming in the vicinity of a sphere. *J. Acoust. Soc. Am.* **27**, 1082–1086 (1955).
30. G. Vishwanathan, G. Juarez, Generation and application of sub-kilohertz oscillatory flows in microchannels. *Microfluid. Nanofluidics* **24**, 69 (2020).
31. K. Chong, S. D. Kelly, S. Smith, J. D. Eldredge, Inertial particle trapping in viscous streaming. *Phys. Fluids* **25**, 033602 (2013).
32. K. Chong, S. D. Kelly, S. T. Smith, J. D. Eldredge, Transport of inertial particles by viscous streaming in arrays of oscillating probes. *Phys. Rev. E* **93**, 013109 (2016).
33. B. R. Lutz, J. Chen, D. T. Schwartz, Hydrodynamic tweezers: 1. Noncontact trapping of single cells using steady streaming microeddies. *Anal. Chem.* **78**, 5429–5435 (2006).
34. W. Strober, Trypan blue exclusion test of cell viability. *Curr. Protoc. Immunol.* **111**, A.3B.1–A.3B.2 (2015).
35. A. Michalczyk, G. Varigos, L. Smith, M. L. Ackland, Fresh and cultured buccal cells as a source of mRNA and protein for molecular analysis. *Biotechniques* **37**, 262–269 (2004).
36. L. B. Leverett, J. D. Hellums, C. P. Alfrey, E. C. Lynch, Red blood cell damage by shear stress. *Biophys. J.* **12**, 257–273 (1972).
37. M. Gazzola, P. Chatelain, W. M. Van Rees, P. Koumoutsakos, Simulations of single and multiple swimmers with non-divergence free deforming geometries. *J. Comput. Phys.* **230**, 7093–7114 (2011).
38. M. Gazzola, C. Mimeau, A. A. Tchieu, P. Koumoutsakos, Flow mediated interactions between two cylinders at finite re numbers. *Phys. Fluids* **24**, 043103 (2012).
39. M. Gazzola, W. M. Van Rees, P. Koumoutsakos, C-start: Optimal start of larval fish. *J. Fluid Mech.* **698**, 5–18 (2012).
40. M. Gazzola, B. Hejazialhosseini, P. Koumoutsakos, Reinforcement learning and wavelet adapted vortex methods for simulations of self-propelled swimmers. *SIAM J. Sci. Comput.* **36**, B622–B639 (2014).
41. M. Gazzola, A. A. Tchieu, D. Alexeev, A. de Brauer, P. Koumoutsakos, Learning to school in the presence of hydrodynamic interactions. *J. Fluid Mech.* **789**, 726–749 (2016).
42. Y. Bhosale, T. Parthasarathy, M. Gazzola, A remeshed vortex method for mixed rigid/soft body fluid-structure interaction. *J. Comput. Phys.* **444**, 110577 (2021).
43. M. R. Maxey, J. J. Riley, Equation of motion for a small rigid sphere in a nonuniform flow. *Phys. Fluids* **26**, 883–889 (1983).
44. J. Towns *et al.*, XSEDE: Accelerating scientific discovery. *Comput. Sci. Eng.* **16**, 62–74 (2014).